Hemispheric Asymmetries in Poynting Flux Derived from DMSP Spacecraft

Delores Knipp,[1,2] Liam Kilcommons,[1] Marc Hairston,[3] and W. Robin Coley[3]

[1]Smead Aerospace Engineering Science Department, University of Colorado Boulder CO USA

[2]High Altitude Observatory, National Center for Atmospheric Research, Boulder CO USA

[3]Space Science Center, University of Texas at Dallas, Richardson Texas USA

Corresponding author: Delores J Knipp (Delores.Knipp@colorado.edu)

Key points:

- Nine-satellite years of DMSP data provide large-scale views of quasi-steady Poynting flux (PF)in each hemisphere, independently
- Stronger solar illumination and magnetic perturbations in the northern hemisphere (NH) appear to be responsible for the PF excess
- During the respective summer seasons in co-sampled regions, the NH receives 25% more PF than the southern hemisphere

Abstract: We provide high-resolution maps of quasi-static Poynting flux (PF) in each hemisphere based on nine-satellite years of Defense Meteorological Satellite Program (DMSP) data. Conjugate comparisons from ~850 km reveal more quasi-static PF arriving in the northern hemisphere (NH) than the southern hemisphere (SH). This tendency is clear in the dawn-dusk sectors and during intervals when Kp < 3, which accounts for ~80% of the study interval. Summer-to-summer comparisons indicate this asymmetry is partially associated with more NH solar illumination, which supports stronger NH field-aligned currents (FAC). Differing hemispheric FAC configurations may also play a role. Our findings support and broaden earlier reports of similar NH preference for the deposition of Alfvenic PF. Regionally the NH has stronger dusk-region PF, while the SH has stronger mid-morning PF. We find PF deposition in the near-cusp regions that rivals and often exceeds the PF intensity in the auroral zones.

Plain Language Summary: One of the responses to solar wind forcing of geospace is the generation of currents that flow along Earth's magnetic fields. These currents exchange information between the magnetosphere and ionosphere about the state of the system. Steady interactions dissipate energy on the large scale as the currents flow through Earth's resistive upper atmosphere. Non-steady interactions also dissipate energy, but on multiple scales as the magnetosphere and ionosphere 'negotiate' how the changes are to be made in the plasmas of both systems. We map medium- and large-scale hemispheric differences in quasi-static electromagnetic energy (Poynting flux--PF) delivered to the two polar regions. On a multi-year basis, the northern hemisphere (NH) receives more electromagnetic energy than the southern hemisphere in almost every sector. Use of nine-satellite years of full-component electric and magnetic field measurements from the Defense Meteorological Satellite Program (DMSP) spacecraft are key to showing medium-sized PF structure near the polar cusps. We show PF deposition in the near-cusp regions that rivals and often exceeds the PF intensity in the auroral zones. Our findings support and broaden a recent report of similar NH preference for the deposition of PF in the noon-midnight meridian.

1. Introduction

The first satellites launched to low Earth orbit (LEO) sparked a flurry of speculation about the energy sources for Earth's heated upper atmosphere. Cole (1962) asserted that Joule heating of the upper atmosphere could explain the fluctuations in orbital acceleration during geomagnetic disturbances. Sugiura (1984, 1986) deduced that high-latitude electric field, **E,** magnetic field, **B**, and their variations d**B**, and d**E,** reported by the Dynamics Explorer-2 (DE-2) mission during a magnetic storm in 1981 were consistent with electromagnetic energy transfer via the Poynting vector and that the transfer was equal to the ionospheric energy (Joule) dissipation below the satellite. Subsequent investigations have considered the Poynting vector, also called Poynting flux (PF), as a source of thermospheric disturbances. The requirement for simultaneous full-component **B**, **E,** d**B**, and d**E** measurements over a range of frequencies and locations has frustrated attempts to systematically quantify PF response to geospace disturbances.

Knudsen (1990) and Kelley et al. (1991) applied Poynting's theorem to HILAT spacecraft measurements (altitude ~800 km) of the convective electric field, **E** and magnetic perturbations d**B** relative to Earth's main field. They calculated electromagnetic energy transfer as:

$$\vec{S} = \frac{-1}{\mu_0}(\vec{E} \times \overrightarrow{\delta B}) \cdot \hat{r} \quad (1)$$

where μ_0 is the permeability in vacuum ($4\pi \times 10^{-7}$ H/m), and the dot product with the radial vector produces energy transfer in the earthward direction. Studying two polar passes, they reported energy transfer of 2-5 mW/m^2 for the field-aligned perturbation Poynting vector, $\mathbf{S}_{\parallel}$, which they called 'Poynting flux.' We adopt the same terminology. Kelley et al. associated this quasi-static PF (scale size ~100's km) with large-scale field aligned currents (FACs) measured near the northern hemisphere (NH) magnetic cusp and in the afternoon auroral zone. At smaller scales (< 10 km) Knudsen et al. [1992] showed that part of the fluctuating electromagnetic energy in the two passes was due to Alfven waves (local δ**E** and δ**B** fluctuations):

$$\vec{S} = \frac{-1}{\mu_0}(\overrightarrow{\delta E} \times \overrightarrow{\delta B}) \cdot \hat{r} \quad (2)$$

where the perturbation vectors are with respect to the average local field.

Gary et al. (1995) provided maps of averaged quasi-static PF distributions from 570 polar passes of the DE-2 LEO mission during its 18-month mission. Visual inspection of their averages for all levels of Kp suggests a hemispherically-integrated PF of ~100 GW and a peak average value of 8 mW/m^2. Olsson et al. (2004) produced similar quasi-static PF distributions from six months (~4000 polar passes) of Astrid-2 data (sorted in two Kp bins). They reported average, peak gridded values of ~ 16 mW/m^2. Both studies were data-limited, so data from both hemispheres were combined for the maps.

In a five-year survey of the nightside auroral zone using Polar and Astrid-2 data, Janhunen et al. (2005) found that Alfvenic PF contributed 0.2-0.3 mW/m^2 while quasi-static PF deposited 1.4-4.0 mW/m^2. with the lower values in each category associated with Kp $\leq$ 2. Hartinger et al. (2015), Hatch et al. (2017) and Keiling et al. (2019) independently reported Alfvenic wave PF above the auroral acceleration region with typical values of 1 mW/m^2. Most of the energy was deposited near the dayside cusp and/or in the nightside substorm region. All studies scaled the Alfvenic PF along magnetic field lines to ~100 km.

Pakhotin et al. (2021) showed significant excess NH Alfvenic-wave PF measured by Swarm spacecraft in the noon-midnight meridian. They reported deposition intensity ≤ 1 mW/m^2. Although we lack uniform coverage in the noon-midnight meridian, we show that the preference for excess NH PF extends to quasi-static PF over broad regions surrounding the dawn-dusk meridian. Below we verify, with a grid resolution of ~220 km and data-averaging scales of ~100 km, the general features of the previous PF studies and discuss hemispheric and longitudinal PF asymmetries that appear in our Kp-based maps. Using nine-satellite years of data from Defense Meteorological Satellite Program (DMSP) spacecraft in three LEO planes we provide the first hemispherically-differentiated patterns of quasi-static PF. In the near-cusp and auroral zones our quasi-static PF is generally 30%-70% higher than reported for Alfvenic-wave PF (e.g., Keiling, 2021 and Pakhotin et al., 2021).

2. Data and Methods

Data Processing. We use DMSP in-situ measurements of ion velocity (**V**) converted to convection **E,** and the FAC-associated d**B,** both at ~850 km to calculate PF using Equation 1. The DMSP F15, F16, and F18 spacecraft are in ~98° inclined, near-circular Sun-synchronous orbits with ~110 min periods. Figure 1 show mean patterns of: a-b) DMSP horizontal components of the ion drift; c-d) FAC-associated d**B;** e-f) the large-scale **E**; g-h) fraction of time PF exceeds 10 mW/m^2 in each bin, when Kp < 3. The bow-tie patterns formed from data acquired in 2011-2014 are the superposition of coverage in magnetic coordinates. Our data processing, described below, is consistent with calculation of 'quasi-static' PF. However, as we discuss in Section 4 there is likely an Alfvenic PF contribution in our results.

The DMSP special sensor for ions electrons and scintillations (SSIES) electric field is calculated as: $\boldsymbol{E} = -\mathbf{v} \times \boldsymbol{B_0}$, where $\boldsymbol{B_0}$ is the International Geomagnetic Reference Field (IGRF) vector at the spacecraft location. The data cadence for F15 is 4-s and for F16 and F18 is 1-s. A corotation **E** is removed during processing. Unlike many previous DMSP PF studies that used only cross-track ion drift (e.g., Knipp et al. 2011; Huang et al. 2017) we use all components of **V**. The Ion Drift Meter (IDM) provides cross-track ion drift, V_y and V_z; while the along-track ion drift, V_x is from current-voltage sweeps from the Retarding Potential Analyzer (RPA). Only drift data designated as Quality Flag (QF) = 1—'good,' are used in this study. To be included, all components of the drift must be simultaneously QF = 1. The quality flags are assigned independently to each of the sensors that measure ion drift (Hairston & Coley, 2019 and Supporting Information, S1). We discard passes with low percentage QF = 1 data. A two-cell convection pattern with convection reversals near 75° magnetic latitude (MLAT) is evident in averaged horizontal drift components in both hemispheres (Fig. 1a-b). The corresponding **E** components are in (Fig. 1e-f). Our results are in good agreement with Jenniges (2015) who independently processed DMSP **E** for the SC 23-24 minimum.

The magnetic perturbations components which we rotate into the SSIES coordinate system (Rich, 1994, p14) are derived at 1-s cadence from the DMSP SSM boom-mounted, triaxial fluxgate magnetometer. We remove the main-field background ($\boldsymbol{B_0} = \mathbf{B}_{IGRF}$) and low-latitude perturbations correlated with the *Dst* as described in Kilcommons et al. (2017) and Burke et al. (2017) to create d**B**. At DMSP altitudes the d**B** due to FACs are typically in the range of 100 - 1000 nT (e.g., Gjerloev et al., 2011). Our averaged values are in the expected range (Fig 1, Row 2). We produce the component of the field-aligned S perpendicular to the ionosphere, S_{down}, following Eqn. 7 of Olsson et al. (2004)

$$S_{down} = \vec{S} \frac{|\vec{B}_{110}|}{|\vec{B}|} \cos(I) \qquad (3)$$

where $\boldsymbol{B}_{110}$ is the measured $\boldsymbol{B}$ adjusted to an altitude of 110 km, I is the inclination angle of the magnetic field at the satellite foot point, and cos (I) produces the PF perpendicular to the ionosphere. Our calculations reveal that hemispherically-integrated S_{down} and $S_{||}$ agree to within ~5%.

To maintain spatial resolution at lower latitudes we used bins of 2° latitude on a side (~220 km) and a width in Magnetic Local Time (MLT), which produces a square-surface area for each bin and 1151 equal-area bins per hemisphere. After making individual PF calculations from only the QF=1 data, we assign the data to appropriate bins. A nominal bin-crossing contains 15 samples of 1-s data (F16 and F18), or ~4 samples of 4-s data (F15). Five hundred bin-crossing segments typically yield > 6000 individual PF measurements. We create averages and standard deviations of all such data segments in the bin and use these statistics as representative of the bin. This result 'standardizes' the data (for instance, removing any need to take the 4-s versus 1-s sampling into account) and produces averages with a spatial scale of ~120 km. This two-step processing reduces the impact of occasional missing values and of high-frequency Alfvenic fluctuations, but does not fully eliminate them. The bottom row of Fig.1 illustrates the bin structure and highlights some of the hemispheric asymmetries we discuss in Sections 3 and 4. The processing described above (and in S1) is an extension of that described in Rastätter et al. (2016) who reported a PF uncertainty of ~2.5 mW/m^2 using the good quality DMSP data.

3. Results

Figure 2 presents Kp-based PF maps for both hemispheres. Figures 2a-b show PF for Kp < 3. Figures 2c-d show the observation density of the ~15-s PF data segments. Aerial coverage is ~10% higher in the SH than in the NH. The NH has a better coverage near noon and hence near the magnetic cusp, but lacks nightside coverage. In contrast, the SH has good nightside coverage. The integrated PF for the coverage in each hemisphere is: 25 GW from 68% coverage in the NH and 29 GW from 78% coverage in the SH. A near-cusp PF of ~3.5 mW/m^2 is present in both hemispheres when Kp < 3 (82% of time during 2011-2014). The auroral regions have ~2mW/m^2 of PF separated from the polar cap PF (< 1 mW/m^2) by 'voids' created by the convection reversals where **E** is approximately zero. Figs 2a-b show features in both hemispheres with aspects in common with 'low-activity' PF patterns in Gary et al. (1995) and Olsson et al. (2004). The former patterns have dayside high-latitude PF and a weak enhancement in the pre-midnight region near 70° MLAT. The Olsson et al. patterns generally have broader and more intense features at slightly lower latitudes. Our auroral region PF is better matched to that in Olsson et al. Our longer sampling time and use of full component drift data seem to better define previously reported large- and medium-scale features.

For Kp $\geq$ 3 (about 18% of the time in 2011-2014), the average patterns are shown in Figs. 2d-e with a color-bar range twice that of Figs. 2a-b. The integrated PF for the covered areas in each hemisphere is: 95 GW (67% coverage) in the NH and 100 GW (75% coverage) in the SH. Both polar caps have a PF intensity of ~ 3-5 mW/m^2. A near-cusp PF of ~7 mW/m^2 is present in the NH when Kp$\geq$3. The centroid of the NH near-cusp PF shifts about 4° equatorward for Kp $\geq$ 3. It is likely that a similar SH shift moves some of the near-cusp PF out of the observation region in the SH. There is a tendency for more PF on the dawn side of the near-cusp region in both hemispheres. This is generally consistent with more complicated high-latitude, morning-side FACs shown by Wing et al. (2010) and with Gary et al. (1995) and Olsson et al. (2004) PF patterns. Where DMSP provides coverage in both hemispheres, our patterns show this tendency is stronger in the SH. The NH auroral regions also show extended regions of PF (> 7 mW/m^2) in the auroral regions with higher intensity tailward of the 06-18 MLT meridian. For nearly all sectors where DMSP coverage overlaps in the two hemispheres, the mean PF is higher in the NH.

The SH auroral PF enhancement is mostly on the dayside consistent with SH dayside FAC enhancements as argued by Liou & Mitchell (2020). The low SH post-midnight PF during high activity may be more of an observational deficit than real. There is a seasonal dependence between Earth's axial tilt and the DMSP orbit planes, such that the SH orbits are more often in darkness. As such, in the dark winter SH the drift measurements are more likely to be discarded due to contamination by the presence of light ions (Anderson, 2001). Nonetheless, the overall tendency for more NH PF is not fully a sampling issue, but rather a physical effect as we discuss next and illustrate in Fig. 3.

We mitigate the hemispheric sampling differences by comparing PF data in conjugate bins for only the local summer months of each hemisphere; that is NH (SH) dipole tilt angle > 0 (< 0). Although the sampling rates are comparable (Figs. 3c-d), the NH still shows more PF than the SH (also evident in Fig 1 g-h). The NH is more illuminated (Figs. 3e-f), especially in the central polar cap. Above 80° MLAT the dayside NH PF is roughly double that in the SH. We suggest the difference is caused by the SH statistical oval and polar cap being slightly shifted with respect to Earth's rotation axis, causing these SH regions to be more in shadow during SH summer solstice. Thus, the NH experiences more solar illumination and has higher conductivity and stronger FACs. In comparing the summer intervals, the PF excess in the NH in the co-sampled regions is 7 GW = (31-24 GW), which is ~25% or ([excess/average] = [7 GW/27.7 GW]). Pakhotin et al. (2021) show a NH excess of Alfvenic PF derived from the Swarm satellite constellation in the noon-midnight meridian of several 10's of percent on average. They associate their result with the SH geomagnetic pole offset.

Figure 4 shows the temporal averages of the binned, PF-related parameters in the co-sampled regions for both hemispheres. Seven-day averages reduce individual-storm influences. Gaps are due to poor quality SSIES measurements in the dark SH. The top panel shows the averages of $|\mathbf{V}|$. The second panel shows $|\mathbf{E}|$, and the third and fourth panel shows averages for $|d\mathbf{B}|$ and PF, respectively. Colored dots correspond to NH-blue and SH-red; black dots correspond to hemispheric differences (scale on the right) with positive being a NH 'excess'. The winter time (dipole tilt negative) enhancement of NH ion drift (Fig. 4a) and **E** (Fig. 4c) are consistent with the radar electric potential results of Pettigrew et al. (2010), who suggested that the Magnetosphere-Ionosphere (M-I) system acts as a current generator with the dark hemisphere having higher **E** to balance low conductivity. Clearly, **E** and PF are out of phase, while d**B** and PF are in phase. The NH average PF 'excess' (~one-third mW/m^2) in the co-sampled bins correlates with the NH FAC 'excess'.

4. Discussion

Nine satellite-years of quality-flagged DMSP drift data allow us to investigate the coincidently-sampled, full-component **E** and d**B** fields at high-latitudes. This is the first global-scale view of high-latitude PF generated independently from DMSP data in both hemispheres. The PF maps reveal hemispheric asymmetries in quasi-static PF both locally and over the entire high-latitude regions.

Regional Hemispheric Comparisons. Figure 1 reveals a notable hemispheric asymmetry in the dusk regions where there are strong NH ion drifts coincident with moderately strong d**B**. Shi et al (2020) show that mean NH AMPERE-derived R1 currents are stronger in the dusk to early-afternoon region. Sangha et al. (2020) show a strong NH-preference for bifurcated substorm Region 2 (R2) FACs that may also contribute to the dusk asymmetry. The PF asymmetry in Fig. 2 scales with geomagnetic activity near dusk and may indicate a mix of dynamic (Alfvenic) and quasi-steady PF signatures.

Figures 2 and 3 indicate strong near-cusp PF in the NH (e.g.,Olsson et al., 2004.) with higher intensities than in Billett et al. (2021). This feature also appears in the SH cusp where satellite coverage exists, although direct comparison is not possible due to limited coverage. Above 80° MLAT this feature is stronger in the NH than the SH. When Kp < 3 this PF feature dominates even the auroral zone PF. When Kp > 3 the near-cusp PF and auroral zone PF are approximately equally intense. Percentage-wise the excess is larger during quiet times.

Figures 2 and 3 also show PF in the high-latitude mid-morning sector that is enhanced in the SH relative to the NH. We believe this is related to the region of relatively intense Region 1 FAC shown in the Shi et al. (2020) Empirical Orthogonal Function analysis of FACs (see their Fig. 1 and Fig. 3 mean patterns). This region overlaps with strong DMSP ion-drift velocity shear. Comparing the pre-dawn sector, the NH PF again exceeds SH PF. This also appears to be the case in the post-midnight/predawn sector for high activity, where the RPA drift data make a significant contribution to **E**. The midnight-sector (only available in the SH) shows little PF, in general agreement with the empirical models of Weimer (2005) and Cosgrove et al. (2014). Hartinger et al. (2015) and Keiling et al. (2019) show this sector to be dominated by substorm-related Alfvenic PF which we have attempted to filter out with averaging.

Figure 4 shows the time series of the averaged parameters related to PF for the co-sampled regions. The enhanced NH d**B** (proxy for FAC) varies directly with the excess NH PF. Coxon et al. (2016) reported that the FAC magnitudes and conductance derived from Iridium AMPERE in the NH are on average greater than the those in the SH. Workayehu et al. (2019) examined nearly 4 years of d**B** measurements from the parallel-flying Swarm A and C satellites. They found the NH FACs to be stronger than the SH FACs by 12% during quiet times. However, during active times they found no significant hemispheric difference in FAC strength. Subsequently Workayehu et al. (2020) reported the asymmetry is seasonal. Zhou & Lühr (2017) used five years of CHAMP data to determine the net ionospheric currents closing FACs. They found weaker net anti-sunward currents in the NH, which they attributed to a smaller conductivity gradient from the auroral oval to the polar cap in the NH. They also found stronger net duskward auroral closing currents in the NH compared to the SH (summer time ratio: NH/SH=1.5) which they associated with an annual higher conductivity in the NH polar region. Stronger NH FACS, as reported here, would also support stronger NH closing currents.

Alfvenic, Quasi-static, Both? From DMSP data we have calculated large-scale, quasi-steady PF, in accordance with the coverage and quality constraints imposed by these data. We find regional PF features that may better align with interpretation as smaller-scale dynamic features consistent with low-frequency Alfven waves. The seasonal variations of **E**, d**B** and PF suggests that we are investigating electromagnetic drivers and PF responses at the quasi-steady/Alfvenic wave interface. Note that Lühr et al. (2015) used a spatial scale of 150 km to separate Swarm mission quasi-static FAC structures from more dynamic structures at smaller scale. McGranaghan et al. (2017) called 150–250 km scale structures, 'mesoscale'. Pakhotin et al. (2019, 2020) argued that dB and FACs with scales < ~ 150 km are more appropriately treated as incident, ionospherically reflected, and interfering Alfvén waves. In their view, an Alfvén wave paradigm could/should be used to accurately describe the entire spectrum of scale sizes involved in MI coupling. Those at larger scale sizes correspond to longer time-scale disturbances. By virtue of our averaging, the perturbations and PF we report are likely in the transition between quasi-static and low-frequency Alfven waves.

The out-of-phase behavior for **E** and d**B** in Fig. 4 is consistent with considering large-scale FACs at a conducting boundary as low-frequency Alfvén waves. For a perfect conductor where the Pedersen conductance becomes infinite at or just above the conductor, $\mathbf{E}_{Tangential} = 0$ while $B_{Tangential}$ is doubled

relative to the incident values far away from the conductor. This condition is realized imperfectly for a good but finite conducting surface such as the summer ionosphere. Note that in the co-sampled summer dawn-dusk regions (Figs. 3e-f) we find an ~7° solar zenith angle difference. For an insulating surface (winter ionosphere), $\mathbf{B}_{Tangential}$ is nulled (or small) and $\mathbf{E}_{Tangential}$ is doubled. See Mallinckrodt & Carlson (1978) for in-depth discussion. Keiling (2009) and Cosgrove (2016) noted that the transition from an Alfvén wave to a quasi-static structure under strong M-I coupling is not fully understood. Seemingly, the ambiguity extends to all levels of activity with implications for regional- (e.g., Lotko & Zhang, 2018) and global-scale energy deposition (this study).

5. Summary and Conclusions

We provide an independent assessment of quasi-static PF in both hemispheres. There are significant regional differences between the two hemispheres that align with previous studies of M-I-coupling phenomena (Section 4). When summer-to-summer comparisons of PF are made in the dawn-dusk regions, the NH sees roughly 25% more PF. We find that the NH tendency for excess PF is associated with stronger FACs in the NH. This may be interpreted as an extension of Alfvenic behavior into what has previously been considered as the 'quasi-static' regime (see Pakhotin et al., 2021). We also find persistent PF in the near-cusp region at a higher intensity than that reported by Billett et al. (2021). For low levels of geomagnetic activity (~80% of the time in this study) the near-cusp PF dominates the auroral zone PF. For Kp $\geq$3 the near-cusp PF can be equal in intensity to auroral PF in the auroral zone. Although we lack full hemispheric coverage, we believe the nine-satellite years of DMSP coincident **E** and d**B** measurements offer important new insights into Poynting flux asymmetry that should be assessed and studied by future LEO missions. In a future manuscript we will present PF maps with an IMF categorization as well as categorization by geomagnetic indices and season.

Acknowledgements

DJK and LMK were supported by AFOSR Award No: FA9550-17-1-0258 and AFOSR MURI Award FA9550-16-1-0364. MH and RC were supported by NASA Grant 80NSSC20K1071. We thank Laila Anderson, William Lotko, Art Richmond and James Slavin for useful discussions. The DMSP drift data are available in the MIT Madrigal database by choosing DMSP at: http://cedar.openmadrigal.org/list
The DMSP magnetometer data, processed in accord with Kilcommons et al. (2017), are available at the NASA https://spdf.gsfc.nasa.gov/pub/data/dmsp/ .

References

Billett, D. D., Perry, G. W., Clausen, L. B. N., Archer, W. E., McWilliams, K. A., Haaland, S., et al. (2021). The relationship between large scale thermospheric density enhancements and the spatial distribution of Poynting flux. *Journal of Geophysical Research: Space Physics*, 126, e2021JA029205. https://doi.org/10.1029/2021JA029205

Burke, W. J., Kilcommons, L. M., and Hairston, M. R. (2017), Storm time coupling between the magnetosheath and the polar ionosphere, *J. Geophys. Res. Space Physics*, 122, 7541– 7554, doi https://doi.org/10.1002/2017JA024101.

Cosgrove, R. B., et al. (2014), Empirical model of Poynting flux derived from FAST data and a cusp signature, J. Geophys. Res., 119, 411–430, doi:10.1002/2013JA019105.

Cosgrove, R. B. (2016) 'Does a localized plasma disturbance in the ionosphere evolve to electrostatic equilibrium? Evidence to the contrary', Journal of Geophysical Research: Space Physics, 121(1), pp. 649-687. doi: 10.1002/2015JA021672.

Coxon, J. C., Milan, S. E., Carter, J. A., Clausen, L. B. N., Anderson, B. J., & Korth, H. (2016). Seasonal and diurnal variations in AMPERE observations of the Birkeland currents compared to modeled results. Journal of Geophysical Research: Space Physics, 121, 4027–4040. https://doi.org/10.1002/2015JA022050

Gary, J. B., Heelis, R. A., Hanson, W. B., and Slavin, J. A. (1994), Field-aligned Poynting Flux observations in the high-latitude ionosphere, *J. Geophys. Res.*, 99(A6), 11417– 11427, doi:10.1029/93JA03167.

Gary, J. B., R. A. Heelis, and J. P. Thayer (1995), Summary of field-aligned Poynting flux observations from DE2, Geophys. Res. Lett., 22(14), 1861–1864, doi:10.1029/95GL00570.

Gjerloev, J. W., S. Ohtani, T. Iijima, B. Anderson, J. Slavin, and G. Le (2011), Characteristics of the terrestrial field-aligned current system, Ann. Geophys., 29, 1713–1729, doi:10.5194/angeo-29-1713-2011

Hairston, Marc, & Coley, W. R. (2019). A Short Introduction to the DMSP SSIES-3 Quality Flags and How to Use Them (Version 1). Zenodo. http://doi.org/10.5281/zenodo.4776161

Hartinger, M. D., M. B. Moldwin, S. Zou, J. W. Bonnell, and V. Angelopoulos (2015), ULF wave electromagnetic energy flux into the ionosphere: Joule heating implications, J. Geophys. Res. Space Physics, 120, 494–510, doi:10.1002/2014JA020129.

Hatch, S. M., LaBelle, J., Lotko, W., Chaston, C. C., & Zhang, B. (2017). IMF control of Alfvénic energy transport and deposition at high latitudes. *Journal of Geophysical Research: Space Physics*, 122, 12,189– 12,211. https://doi.org/10.1002/2017JA024175

Huang, C. Y., Huang, Y., Su, Y.-J., Hairston, M. R., and Sotirelis, T. (2017). DMSP observation of high latitude Poynting Flux during magnetic storm, Journal of Atmospheric and Solar - Terrestrial Physics,164, 294–307. https://doi.org/10.1016/j.jastp.2017.09.005

Janhunen, P, A. Olsson N. A. Tsyganenko, C. T. Russell, H. Laakso, and L.G. Blomberg, (2005), Statistics of a parallel Poynting vector in the auroral zone as a function of altitude using Polar EFI and MFE data and Astrid-2 EMMA data, Annales Geophysicae, 23, 1797–1806, 2005

Jenniges, Janelle V., (2015), A Study of the Dayside High-Latitude Ionospheric Electrodynamics During Extended Solar Minimum, All Graduate Theses and Dissertations. 4481. https://digitalcommons.usu.edu/etd/4481

Keiling, A., (2009), Alfvén waves and their roles in the dynamics of the Earth's magnetotail: a review. Space Sci. Rev. 142, 73–156. https://doi.org/10.1007/ s11214-008-9463-8.

Keiling, A., (2021), The dynamics of the Alfvénic oval, Journal of Atmospheric and Solar - Terrestrial Physics, DOI:10.1016/J.JASTP.2021.105616

Keiling, A., S. Thaller, J. Wygant, and J. Dombeck (2019), Assessing the global Alfven wave power flow into and out of the auroral acceleration region during geomagnetic storms, Sci. Adv Vol. 5, no. 6, eaav8411,DOI: 10.1126/sciadv.aav8411

Kelley, M. C., Knudsen, D. J., & Vickrey, J. F. (1991). Poynting flux measurements on a satellite: A diagnostic tool for space research. Journal of Geophysical Research, 96(A1), 201–207. https://doi.org/10.1029/90JA01837.

Kilcommons, L. M., R. J. Redmon, and D. J. Knipp (2017), A new DMSP magnetometer & auroral boundary dataset and estimates of field aligned currents in dynamic auroral boundary coordinates, *J. Geophys. Res. Space Physics*, 122, doi:10.1002/2016JA023342

Knipp, D., S. Eriksson, L. Kilcommons, G. Crowley, J. Lei, M. Hairston, and K. Drake. Extreme Poynting flux in the dayside thermosphere: examples and statistics. Geophys. Res. Lett., 38, L16102, 2011,DOI: 10.1029/2011GL048302.

Knipp, D. J., L. M. Kilcommons, J. Gjerloev, R. J. Redmon, J. Slavin, and G. Le (2015), A large-scale view of Space Technology 5 magnetometer response to solar wind drivers, Earth and Space Science, 2, doi:10.1002/2014EA000057.

Knudsen, D. J., Alfven waves and static fields in magnetosphere/ionosphere coupling: In-situ measurements and a numerical model, Ph.D. thesis, Cornell Univ., Ithaca, N.Y., 1990. https://apps.dtic.mil/sti/pdfs/ADA356871.pdf.

Knudsen, D. J., Kelley, M. C., and Vickrey, J. F. (1992), Alfvén waves in the auroral ionosphere: A numerical model compared with measurements, *J. Geophys. Res.*, 97(A1), 77– 90, doi:10.1029/91JA02300.

Landry, R. G., & Anderson, P. C. (2018).An Auroral boundary-oriented model of subauroral polarization streams (SAPS).Journal of Geophysical Research: SpacePhysics,123, 3154–3169. https://doi.org/10.1002/2017JA024921

Liou, K. & Mitchell, E.J. Hemispheric asymmetry of the dayside aurora due to imbalanced solar insolation. *Sci Rep* **10,** 13451 (2020). https://doi.org/10.1038/s41598-020-70018-w

Lotko, W., & Zhang, B. (2018). Alfvénic heating in the cusp ionosphere-thermosphere. *Journal of Geophysical Research: Space Physics*, 123, 10,368– 10,383. https://doi.org/10.1029/2018JA025990

Lühr, H., Park, J., Gjerloev, J. W., Rauberg, J., Michaelis, I., Merayo, J. M. G., & Brauer, P. (2015). Field-aligned currents' scale analysis performed with the Swarm constellation. Geophysical Research Letters, 42, 1–8. https://doi.org/10.1002/2014GL062453

Mallinckrodt, A. J., and Carlson, C. W. (1978), Relations between transverse electric fields and field-aligned currents, *J. Geophys. Res.*, 83(A4), 1426– 1432, doi:10.1029/JA083iA04p01426.

McGranaghan, R. M., Mannucci, A. J., & Forsyth, C. (2017). A comprehensive analysis of multiscale field-aligned currents: Characteristics, controlling parameters, and relationships. *Journal of Geophysical Research: Space Physics*, 122, 11,931– 11,960. https://doi.org/10.1002/2017JA024742

Olsson, A., P. Janhunen, T. Karlsson, N. Ivchenko, and L. G. Blomberg (2004), Statistics of joule heating in the auroral zone and polar cap using Astrid-2 satellite Poynting flux, Ann. Geophys., 22, 4133–4142, https://doi.org/10.5194/angeo-22-4133-2004.

Pakhotin, I. P., Mann, I. R., Lysak, R. L., Knudsen, D. J., Gjerloev, J. W., Rae, I. J., et al. (2018). Diagnosing the role of Alfvén waves in magnetosphere ionosphere coupling: Swarm observations of large amplitude nonstationary magnetic perturbations during an interval of northward IMF. Journal of Geophysical Research: Space Physics, 123, 326–340. https://doi.org/10.1002/2017JA024713

Pakhotin, I. P., Mann, I. R., Knudsen, D. J., Lysak, R. L., & Burchill, J. K. (2020). Diagnosing the role of Alfvén waves in global field-aligned current system dynamics during southward IMF: swarm observations. Journal of Geophysical Research: Space Physics, 125, e2019JA027277. https://doi.org/ 10.1029/2019JA027277

Pakhotin, I.P., Mann, I.R., Xie, K. et al., (2021) Northern preference for terrestrial electromagnetic energy input from space weather. Nat Commun 12, 199. https://doi.org/10.1038/s41467-020-20450-3.

Pettigrew, E. D., Shepherd, S. G., and Ruohoniemi, J. M. (2010), Climatological patterns of high-latitude convection in the Northern and Southern hemispheres: Dipole tilt dependencies and interhemispheric comparisons, *J. Geophys. Res.*, 115, A07305, doi:10.1029/2009JA014956.

Rastätter L., et al. (2016), GEM-CEDAR challenge: Poynting flux at DMSP and modeled Joule heat, Space Weather,14, doi:10.1002/2015SW001238

Sangha, H., Milan, S. E., Carter, J. A., Fogg, A. R., Anderson, B. J., Korth, H., & Paxton, L. J. (2020). Bifurcated Region 2 field-aligned currents associated with substorms. *Journal of Geophysical Research: Space Physics*, 125, e2019JA027041. https://doi.org/10.1029/2019JA027041

Shi, Y., Knipp, D. J., Matsuo, T., Kilcommons, L., & Anderson, B. (2020). Modes of (FACs) variability and their hemispheric asymmetry revealed by inverse and assimilative analysis of iridium magnetometer data. Journal of Geophysical Research: Space Physics, 125, e2019JA027265. https://doi.org/10.1029/2019JA027265

Sugiura, M. (1984), A fundamental magnetosphere-Ionosphere coupling mode involving field-aligned currents as deduced from DE-2 observations. Geophys. Res. Lett, 11: 877-880. doi:10.1029/GL011i009p00877

Sugiura, M. (1986), Joule heating and field-aligned currents: Preliminary results from DE-2, https://ntrs.nasa.gov/archive/nasa/casi.ntrs.nasa.gov/19860019864.pdf

Weimer, D. R. (2005), Improved ionospheric electrodynamic models and application to calculating Joule heating rates, J. Geophys. Res., 110, 10.1029/2004JA010884

Wing, S., Ohtani, S., Newell, P. T., Higuchi, T., Ueno, G., and Weygand, J. M. (2010), Dayside field-aligned current source regions, *J. Geophys. Res.*, 115, A12215, doi: https://doi.org/10.1029/2010JA015837.

Workayehu, A. B., Vanhamäki, H., & Aikio, A. T. (2019). Field-aligned and horizontal currents in the Northern and Southern Hemispheres from the Swarm satellite. Journal of Geophysical Research: Space Physics, 124, 7231–7246. https://doi.org/10.1029/2019JA026835

Workayehu, A. B., Vanhamäki, H., & Aikio, A. T. (2020). Seasonal effect on hemispheric asymmetry in ionospheric horizontal and field-aligned currents. Journal of Geophysical Research: Space Physics, 125, e2020JA028051. https://doi.org/10.1029/2020JA028051

Zhang, X.-X., He, F., Wang, W., and Chen, B. (2015), Hemispheric asymmetry of subauroral ion drifts: Statistical results. *J. Geophys. Res. Space Physics*, 120, 4544– 4554. doi: 10.1002/2015JA021016.

Zhou, Y.-L., & Lühr, H. (2017), Net ionospheric currents closing field-aligned currents in the auroral region: CHAMP results, *J. Geophys. Res. Space Physics*, 122, 4436– 4449, doi:10.1002/2016JA023090.

Figure Captions

*Figure 1. DMSP data for Kp < 3. The dial plots display the NH (left) and the SH (right). Top row a-b: convection velocity; Second row c-d: magnetic perturbations; Third row e-f: convection **E**; Fourth row g-h: percent of time PF exceeds 10 mW/m^2. Magnitude corresponds to arrow length, and is further highlighted according to the purple-gray color bar. Data are mapped to 110 km. The outer ring is 50 deg MLAT. Noon is at the top.*

Figure 2. a-b) Polar plots of NH and SH PF for Kp < 3. The color bar is in mW/m^2; Integrated power is in GW; c-d) Polar plots of data coverage, with percent coverage; e-f) Polar plots of NH and SH PF for Kp ≥ 3; g-h) Polar plots of data coverage.

Figure 3. a-b) Hemispherically-conjugate bins of average PF for summer conditions where the seasonal component of dipole angle > 0 for NH and dipole angle < 0 for SH; c-d) Percent for bins containing more than 100 passes; e-f) Average solar zenith angle; g-h) Standard deviation of solar zenith angle in degrees.

*Figure 4. Seven-day averages of the magnitude of the DMSP **V**, **E**, d**B**, and PF, calculated for the co-sampled bins in Figure 3. Magnitude scales are on the left. Blue - NH data: Red - SH data. Differences in each parameter are shown in black (note the scale is on the right), with positive black values indicating a NH 'excess'. Gaps are present during SH winter when the drift data suffer light-ion contamination.*

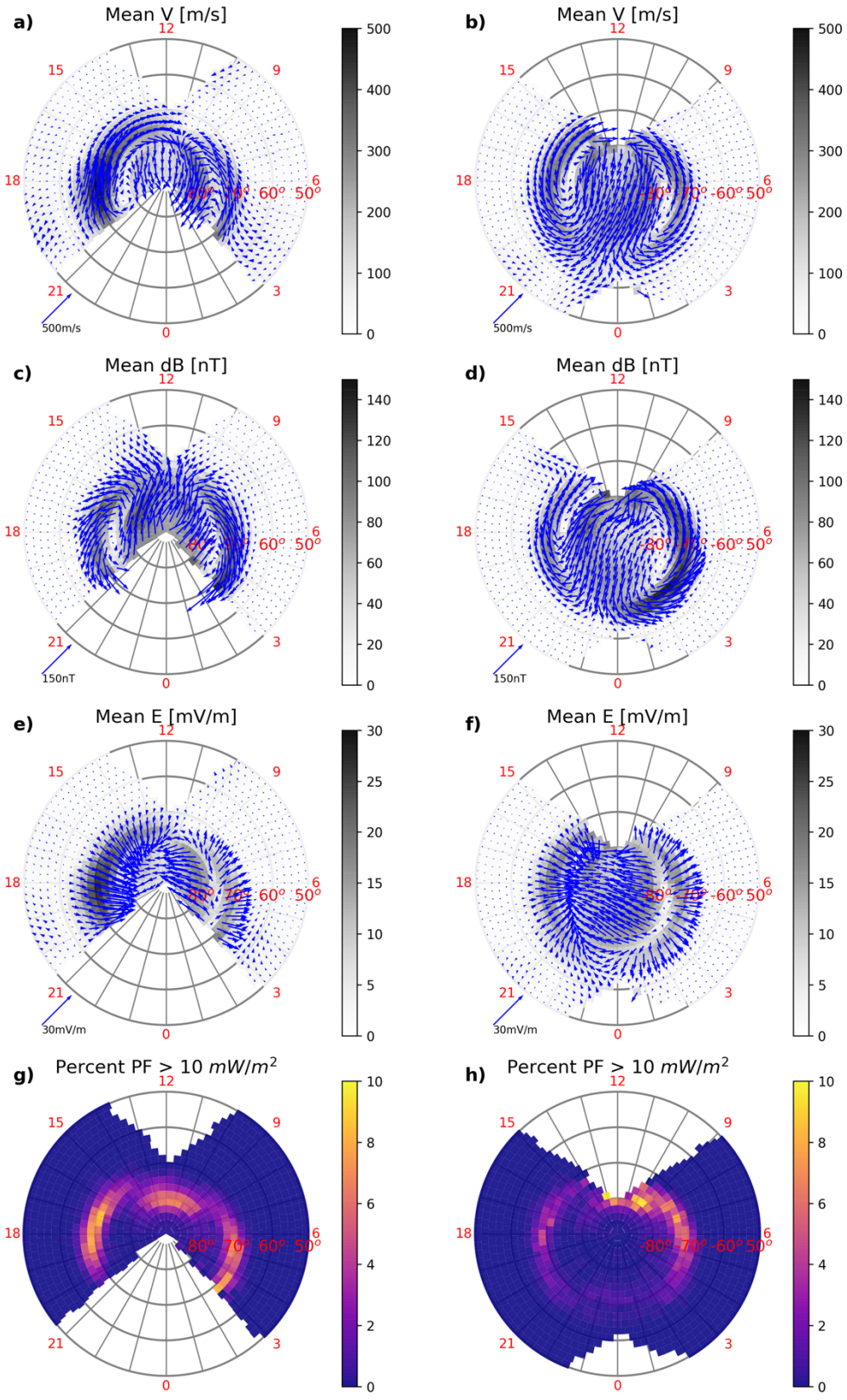
a)
Mean V [m/s]
500m/s
b)
Mean V [m/s]
500m/s
c)
Mean dB [nT]
150nT
d)
Mean dB [nT]
150nT
e)
Mean E [mV/m]
30mV/m
f)
Mean E [mV/m]
30mV/m
g)
Percent PF > 10 mW/m²
h)
Percent PF > 10 mW/m²

Figure 1

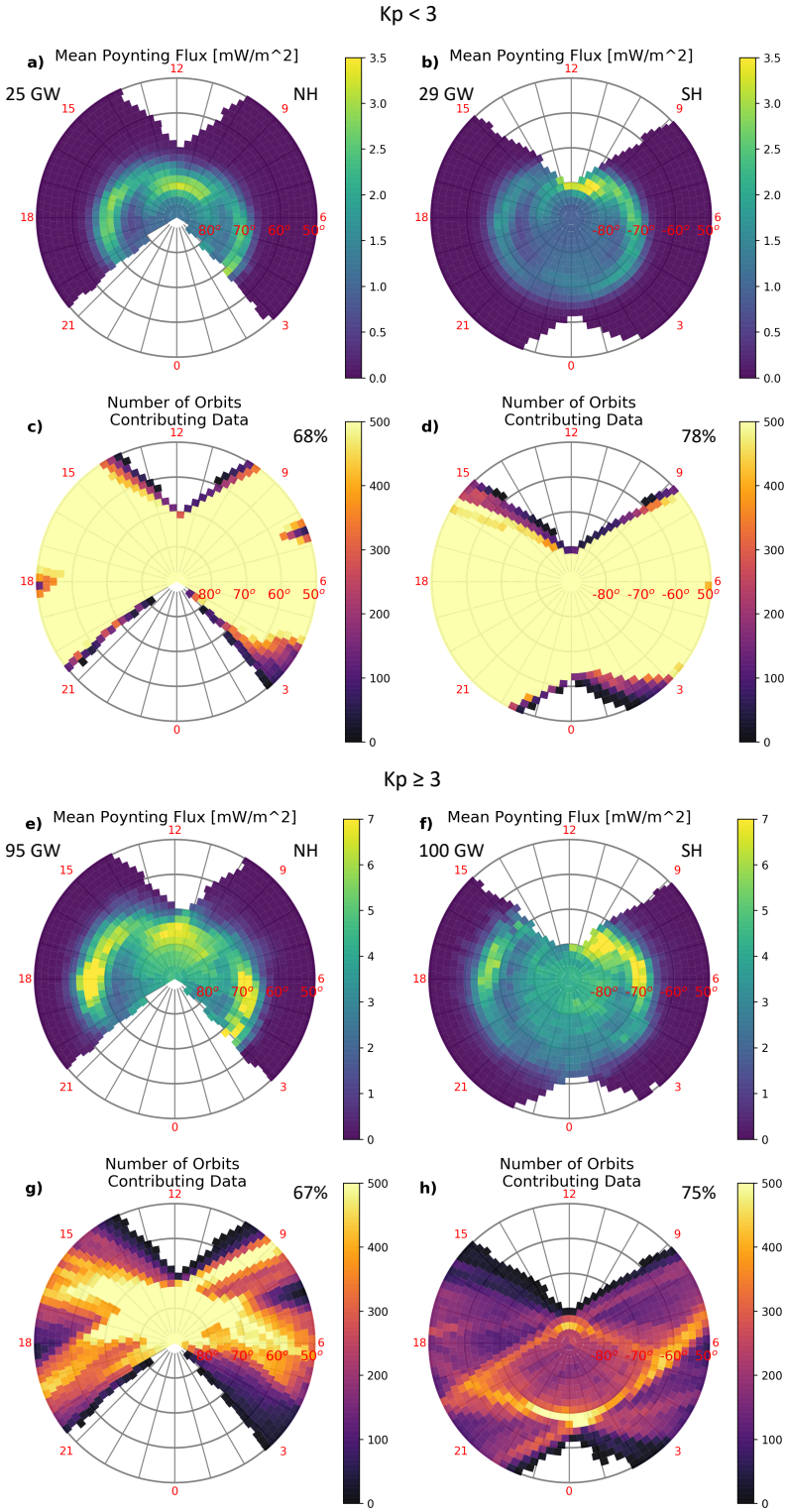
Kp < 3
a) Mean Poynting Flux [mW/m^2]
25 GW
NH
b) Mean Poynting Flux [mW/m^2]
29 GW
SH
c) Number of Orbits Contributing Data
68%
d) Number of Orbits Contributing Data
78%
Kp ≥ 3
e) Mean Poynting Flux [mW/m^2]
95 GW
NH
f) Mean Poynting Flux [mW/m^2]
100 GW
SH
g) Number of Orbits Contributing Data
67%
h) Number of Orbits Contributing Data
75%
-80° -70° -60° -50°

Figure 2

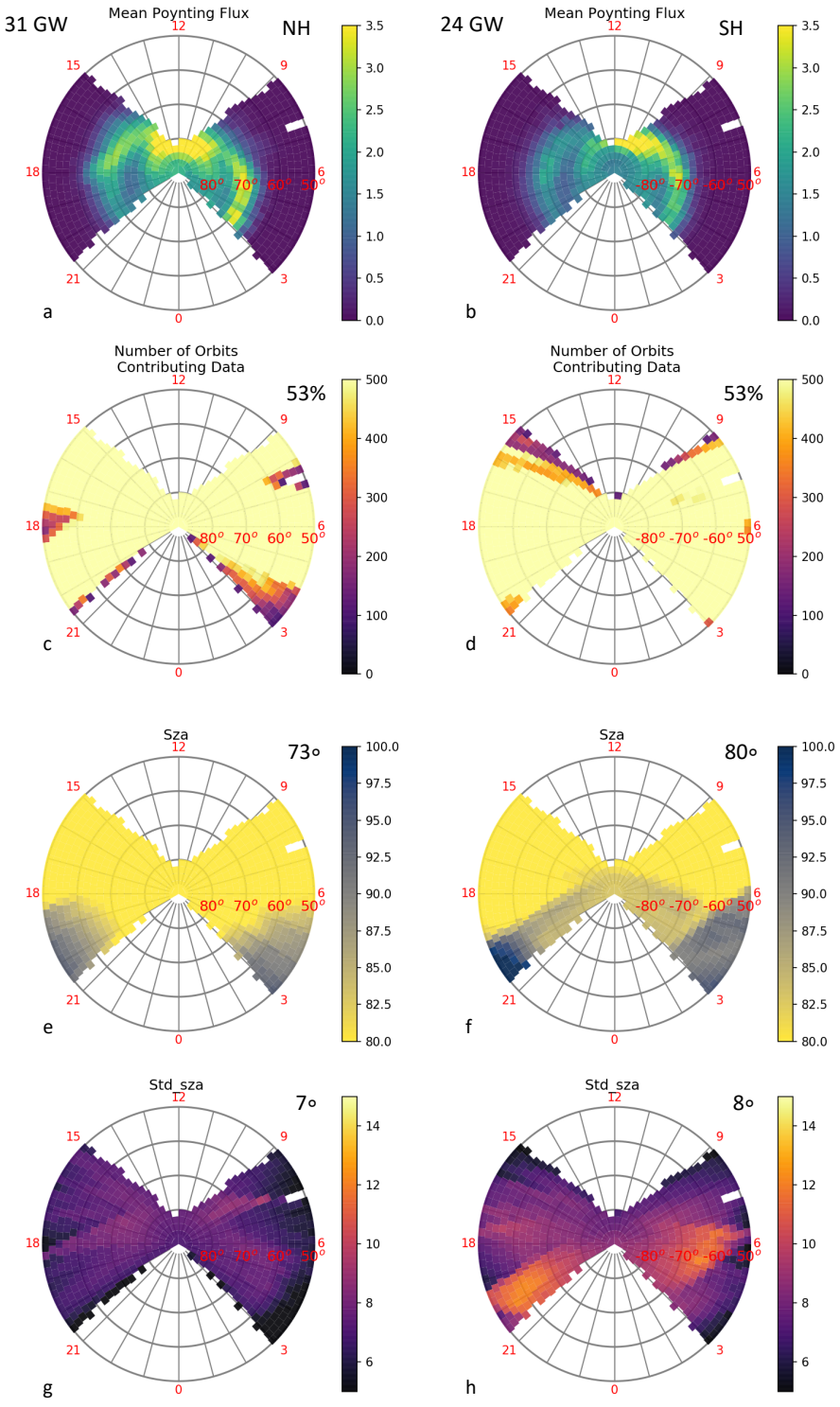
31 GW
Mean Poynting Flux
NH
24 GW
Mean Poynting Flux
SH
a
b
Number of Orbits
Contributing Data
53%
c
Number of Orbits
Contributing Data
53%
d
Sza
73°
e
Sza
80°
f
Std_sza
7°
g
Std_sza
8°
h

Figure3

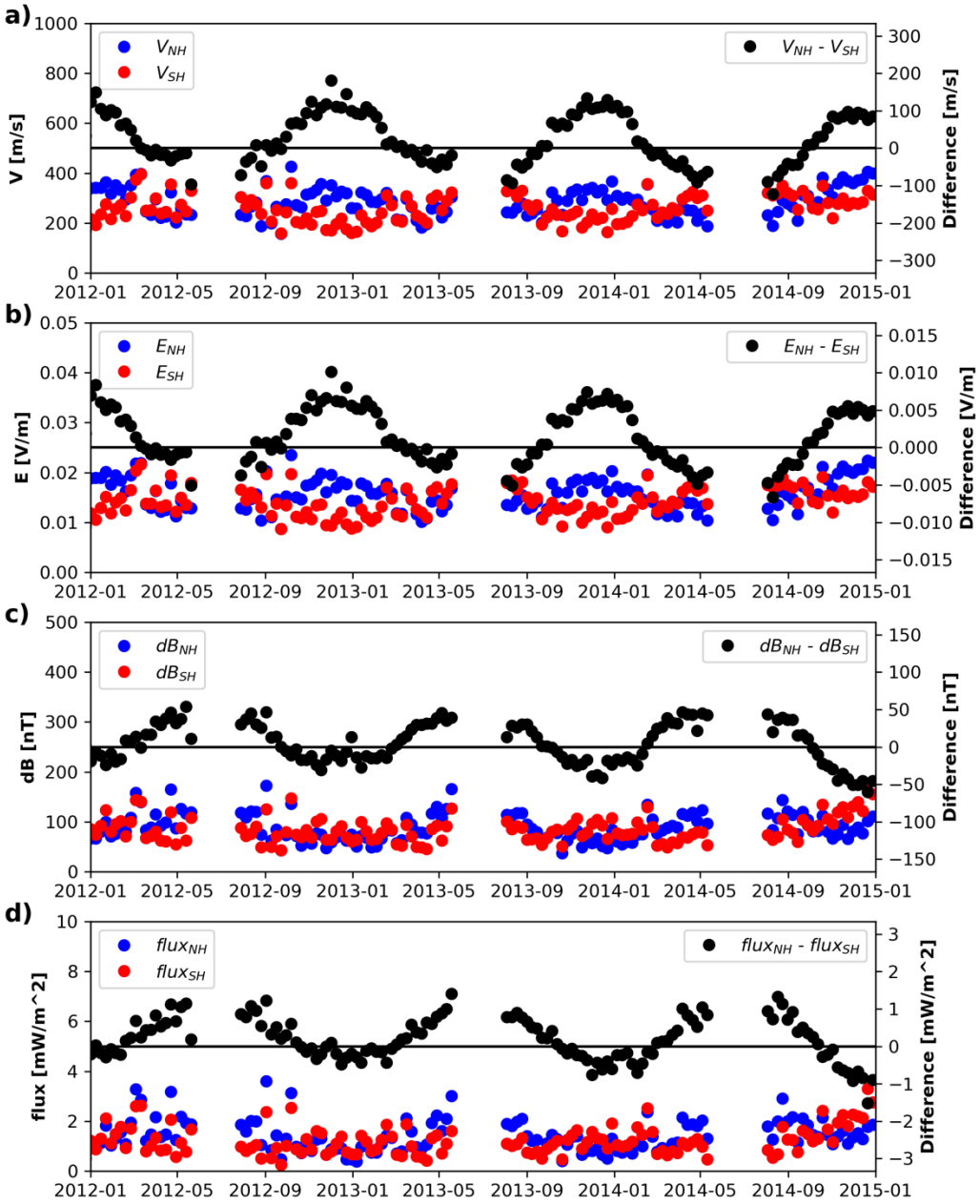
a)
V_{NH}
V_{SH}
V_{NH} - V_{SH}
V [m/s]
Difference [m/s]
b)
E_{NH}
E_{SH}
E_{NH} - E_{SH}
E [V/m]
Difference [V/m]
c)
dB_{NH}
dB_{SH}
dB_{NH} - dB_{SH}
dB [nT]
Difference [nT]
d)
$flux_{NH}$
$flux_{SH}$
$flux_{NH}$ - $flux_{SH}$
flux [mW/m^2]
Difference [mW/m^2]
2012-01
2012-05
2012-09
2013-01
2013-05
2013-09
2014-01
2014-05
2014-09
2015-01

Figure 4

Geophysical Research Letters

Supporting Information for

Hemispheric Asymmetries in Poynting Flux Derived from DMSP Spacecraft

Delores Knipp,[1,2] Liam Kilcommons,[1] Marc Hairston,[3] and W. Robin Coley[3]

[1]Smead Aerospace Engineering Science Department, University of Colorado Boulder CO USA

[2]High Altitude Observatory, National Center for Atmospheric Research, Boulder CO USA

[3]Space Science Center, University of Texas at Dallas, Richardson Texas USA

Corresponding author: Delores J Knipp (Delores.Knipp@colorado.edu)

Contents of this file

Introduction

This supplemental text contains short sections describing: 1) Defense Meteorological System Program (DMSP) Special Sensor Ions Electrons and Scintillation (SSIES) Quality Flags; 2) DMSP SSIES Baseline Removal Method; and 3) Uncertainty discussion related to the DMSP magnetic perturbation estimates. It also contains one Figure showing DMSP observation distribution.

Text S1.

SSIES Quality Flags: The DMSP ion flows are measured by the special sensor-ion electrons scintillation (SSIES) instruments on board the spacecraft. DMSP-F15 carried the SSIES-2 version of the instrument package while DMSP-F16 and later spacecraft carried the more advanced SSIES-3 version. Thus, the determination of the quality flags (good, caution, poor) for the data are slightly different between the two versions. For SSIES-2 the velocities were measured on a 4-second cadence (~30 km) to match the 4-second sweep of the Retarding Potential Analyzer (RPA) which gives the in-track flow (V_{Along}). The SSIES-3 velocities are on a 1-second cadence.

The Ion Drift Meter (IDM) samples the cross-track flow (V_{Cross}) six times a second and takes the average of these measurements to produce the corresponding V_{Cross} value. The RPA calculates the in-track flow by measuring the amount of ion current into the instrument as a function of a varying retarding potential placed on a grid at the RPA's opening, then fitting a Maxwellian function to the resulting current-voltage curve. Assuming the plasma is relatively uniform throughout the retarding potential sweep, the Maxwellian distribution of the ion energy is reasonable and the fit should be good.

From this fit, the in-track flow velocity, the ion temperature, the ion density, and the fractional composition of the O+, He+, and H+ in the plasma are determined (see *Rich*, 1994 and *Heelis and Hanson*, 1998 for more details). The quality flag on the in-track flow is based on the RMS error of the fit to the data curve. The good quality flag for the V_{Cross} values indicates the sweeps where the RMS error was low enough for all the parameters from the RPA to be determined. The IDM was designed to work optimally in a moderate to high density plasma that is predominately composed of O+ ions. Under conditions where the total ion density was at least 10^3 ions/cc and the O+ fraction of the ions (as measured by the RPA) was 85% or higher, the V_{Cross} values are flagged as 'Good.' Only the F15 SSIES-2 data for which both velocity values were flagged as Good (Quality Flag = 1) were used in this analysis

The basic mechanics of the measurements by the SSIES-3 instrument package are the same as the SSIES-2 except that the sweep time for the RPA has been shortened to 1 second, thus the cadence of the flow data is now 1 second (~ 7.5 km) with 6 measurements of the cross-track flow going into the averaged V_{Cross} value. The quality flag algorithm for the RPA is more sophisticated with separate flags for each of the parameters. For the V_{Along} quality flag to be rated as good, the RMS fit of the curve to the data must be less than or equal to 0.12 and the resulting V_{Along} value is between -1000 and +1000 m/s. For the SSIES-3 IDM the quality flags were revised to accept slightly lower O+ fractional compositions so long as the ion densities were in the high range. The V_{Cross} measured values were flagged as good if the O+ fraction was greater than 75% (as measured by the RPA) and the total ion density was greater than 10^3 ions/cm^3. As with F15, only the F16 and F18 data where both velocity values were flagged as good were used in this analysis. See *Hairston and Coley* (2019) for more details

SSIES Baseline Removal: The IDM faces the spacecraft ram direction to within 0.5° inclination. Errors in the drifts due to the offset are of the order of 100 s of m/s, necessitating a baseline removal. As in *Zhu et al.* (2021*)* linear baseline corrections of V_x, V_y, and V_z components are applied to ensure they are zero at both ends of each polar crossing (i.e., |MLAT| = 45° in this study). For this study corrections are performed automatically with a weighted least-squares regression, using weights which penalize low quality measurements. (We do permit use of QF =2 data for baseline determination.) *Landry & Anderson* (2018) note that automated baseline correction algorithms can be off by as much as 100 m/s from a manually selected baseline, so a statistical collection of DMSP measurements should be considered to have a resolution limit of ~100 m/s. There are systematic uncertainties in the accuracy of the cross-track flows in the F17 data so these data were not included in this study.

Data Reliability. Although we have implemented a number of quality control measures in including the full-component DMSP **E,** and d**B** on a large scale, the nature of operational spacecraft data adds uncertainty**.** Appendix A of *Rastätter et al.* (2016) contains an extended discussion of Estimating Error Levels of DMSP Poynting Flux. An estimate of 2.5 mW/m^2 was determined based on use of QF =1 data from RPA and IDM observations. For auroral zone PF values of 10 mW/m^2 this translate` to ~25% uncertainty (and 60-70%% uncertainty in regions of low intensity PF.)

The DMSP magnetometer has an uncertainty of +/- 2 nT, however slight boom misalignments during flight are known to occur. See *Knipp et al.* (2015) and *Kilcommons et al.* (2017) for more details. For our study the mostly likely source of error is in removal of the background field. The locations of the spacecraft is only recorded each minute. Intermediate locations are determined via orbit propagation, often producing a 1 s to 2 s error, which translates to a likely IGRF background removal uncertainty of 100 nT.

The DE-2 spacecraft experienced systematic roll errors in the horizon sensor of up to several times 0.1 deg. *Gary et al.* (1994) estimated a maximum cumulative uncertainty of 50 nT for the DE-2 d**B**, and a cumulative uncertainty of 2 mV/m for **E**. They reported PF error of 60% in regions with low intensity PF, whereas in the typical auroral zone they estimated ~14% uncertainty in PF.

The uncertainty for DMSP PF is of the same magnitude as that reported by *Gary et al (1994)*. We have approximately two orders of magnitude more data than shown in Gary et al. We believe the large amount of data helps to mitigate the uncertainty described above.

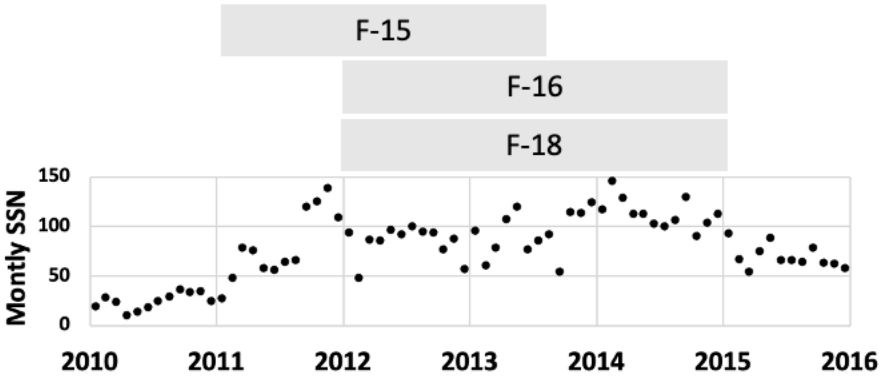

Figure S1. Distribution of DMSP data used in this study for the rise and peak of solar cycle 24.

References

Gary, J. B., Heelis, R. A., Hanson, W. B., and Slavin, J. A. (1994), Field-aligned Poynting Flux observations in the high-latitude ionosphere, *J. Geophys. Res.*, 99(A6), 11417– 11427, doi:10.1029/93JA03167.

Hairston, Marc, & Coley, W. R. (2019). A Short Introduction to the DMSP SSIES-3 Quality Flags and How to Use Them (Version 1). Zenodo. http://doi.org/10.5281/zenodo.4776161

Heelis, R.A. and Hanson, W.B. (1998). Measurements of Thermal Ion Drift Velocity and Temperature Using Planar Sensors. In Measurement Techniques in Space Plasmas: Particles (eds R.F. Pfaff, J. Borovsky and D.T. Young). https://doi.org/10.1029/GM102p0061

Knipp, D. J., Matsuo, T., Kilcommons, L., Richmond, A., Anderson, B., Korth, H., Redmon, R., Mero, B., and Parrish, N. (2014), Comparison of magnetic perturbation data from LEO satellite constellations: Statistics of DMSP and AMPERE, *Space Weather*, 12, 2– 23, doi:10.1002/2013SW000987.

Landry, R. G., & Anderson, P. C. (2018). An Auroral boundary-oriented model of subauroral polarization streams (SAPS). *Journal of Geophysical Research: Space Physics*, 123, 3154– 3169. https://doi.org/10.1002/2017JA024921

Rastätter, L., Shim, J. S., Kuznetsova, M. M., Kilcommons, L. M., Knipp, D. J., Codrescu, M., Fuller-Rowell, T., Emery, B., Weimer, D. R., Cosgrove, R., et al. (2016), GEM-CEDAR challenge: Poynting flux at DMSP and modeled Joule heat, *Space Weather*, 14, 113– 135, doi:10.1002/2015SW001238.

Rich, F. (1994), User's guide for the topside ionospheric plasma monitor (SSIES, SSIES -2 and SSIES-3) on spacecraft of the defense meteorological satellite program (DMSP). volume 1; Technical description, PLTR 942187, Directorate of Geophysics AIR FORCE MATERIEL COMMAND HANSCOM AFB, MA 01731-3010, https://satdat.ngdc.noaa.gov/dmsp/docs/Rich%20-%201994%20-%20Users%20Guide%20SSIES-1%20SSIES-2%20SSIES-3%20-%20PL-TR-94-2187.pdf

Zhu, Q., Deng, Y., Maute, A., Kilcommons, L., Knipp, D., & Hairston, M. (2021). ASHLEY: A new empirical model for the high-latitude electron precipitation and electric field. *Space Weather*, 19, e2020SW002671. https://doi.org/10.1029/2020SW002671